Compressive Hyperspectral Imaging via Approximate Message Passing

Jin Tan, *Student Member, IEEE*, Yanting Ma, *Student Member, IEEE*, Hoover Rueda, *Student Member, IEEE*, Dror Baron, *Senior Member, IEEE*, and Gonzalo R. Arce, *Fellow, IEEE*

Abstract

We consider a compressive hyperspectral imaging reconstruction problem, where three-dimensional spatio-spectral information about a scene is sensed by a coded aperture snapshot spectral imager (CASSI). The CASSI imaging process can be modeled as suppressing three-dimensional coded and shifted voxels and projecting these onto a two-dimensional plane, such that the number of acquired measurements is greatly reduced. On the other hand, because the measurements are highly compressive, the reconstruction process becomes challenging. We previously proposed a compressive imaging reconstruction algorithm that is applied to two-dimensional images based on the approximate message passing (AMP) framework. AMP is an iterative algorithm that can be used in signal and image reconstruction by performing denoising at each iteration. We employed an adaptive Wiener filter as the image denoiser, and called our algorithm "AMP-Wiener." In this paper, we extend AMP-Wiener to three-dimensional hyperspectral image reconstruction. Applying the AMP framework to the CASSI system is challenging, because the matrix that models the CASSI system is highly sparse, and such a matrix is not suitable to AMP and makes it difficult for AMP to converge. Therefore, we modify the adaptive Wiener filter to fit the three-dimensional image denoising problem, and employ a technique called damping to solve for the divergence issue of AMP. Our simulation results show that AMP-Wiener in three-dimensional hyperspectral imaging problems outperforms existing widely-used algorithms such as gradient projection for sparse reconstruction (GPSR) and two-step iterative shrinkage/thresholding (TwIST) given the same amount of runtime. Moreover, in contrast to GPSR and TwIST, AMP-Wiener need not tune any parameters, which simplifies the reconstruction process.

Index Terms

Approximate message passing, CASSI, compressive hyperspectral imaging, gradient projection for sparse reconstruction, image denoising, two-step iterative shrinkage/thresholdng, Wiener filtering.

The work of Jin Tan, Yanting Ma, and Dror Baron was supported in part by the National Science Foundation under the Grant CCF-1217749 and in part by the U.S. Army Research Office under the Grant W911NF-14-1-0314. The work of Hoover Rueda and Gonzalo R. Arce was supported by the U.S. Army Research Office under the contract W911NF-12-1-0380.

Jin Tan, Yanting Ma, and Dror Baron are with the Department of Electrical and Computer Engineering, NC State University, Raleigh, NC 27695. E-mail: {jtan, yma7, barondror}@ncsu.edu. Hoover Rueda and Gonzalo R. Arce are with the Department of Electrical and Computer Engineering, University of Delaware, Newark, DE 19716. E-mail: {rueda,arce}@udel.edu.

I. Introduction

A. Motivation

A hyperspectral image is a three-dimensional (3D) image cube comprised of a collection of two-dimensional (2D) images (slices), where each 2D image is captured at a specific wavelength. Hyperspectral images allow us to analyze spectral information about each spatial point in a scene, and thus can help us identify different materials that appear in the scene. Therefore, hyperspectral imaging has applications to areas such as medical imaging [1, 2], remote sensing [3], geology [4], and astronomy [5].

Conventional spectral imagers include whisk broom scanners, push broom scanners [6, 7], and spectrometers [8]. In whisk broom scanners, a mirror reflects light onto a single detector, so that one pixel data is collected at a time; in push broom scanners, an image cube is captured with one focal plane array (FPA) measurement per spatial line of the scene; and in spectrometers, a set of optical bandpass filters are tuned in steps in order to scan the scene. The disadvantages of these techniques are that (i) data acquisition takes a long time, because they require scanning a number of zones linearly in proportion to the desired spatial and spectral resolution; and (ii) large amounts of data are acquired and must be stored and transmitted.

To address the limitations of conventional spectral imaging techniques, many spectral imager sampling schemes based on compressive sensing [9–11] have been proposed [12–14]. The coded aperture snapshot spectral imager (CASSI) [12, 15–17] is a popular compressive spectral imager and acquires image data from different wavelengths simultaneously. In CASSI, the voxels of a scene are first coded by an aperture, then dispersed by a dispersive element, and finally detected by a 2D FPA. That is, a 3D image cube is suppressed and measured by a 2D array, and thus CASSI acquires far fewer measurements than those acquired by conventional spectral imagers, which significantly accelerates the imaging process. On the other hand, because the measurements from CASSI are highly compressive, reconstructing 3D image cubes from CASSI measurements becomes challenging. Moreover, because of the massive size of 3D image data, it is desirable to develop fast reconstruction algorithms in order to realize real time acquisition and processing.

Fortunately, it is possible to reconstruct the 3D cube from the 2D measurements according to the theory of compressive sensing [9–11], because the 2D images from different wavelengths are highly correlated, and the 3D image cube is sparse in an appropriate transform domain, meaning that only a small portion of the transform coefficients have large values. Approximate message passing (AMP) [18] has recently become a popular algorithm that solves for compressive sensing problems, owing to its promising performance and efficiency. Therefore, we are motivated to investigate how to apply AMP to the CASSI system.

B. Related work

Several algorithms have been proposed to reconstruct image cubes from measurements acquired by CASSI. One of the efficient algorithms is gradient projection for sparse reconstruction (GPSR) [19], which is fast and usually produces reasonable reconstruction. GPSR models hyperspectral image cubes as sparse in the Kronecker product

of a 2D wavelet transform and a 1D discrete cosine transform (DCT), and solves the regularized ℓ_1-minimization problem to enforce sparsity in this transform domain. Besides using ℓ_1-norm as the regularizer, total variation is a popular alternative; Wagadarikar et al. [15] employed total variation [20, 21] as the regularizer in the two-step iterative shrinkage/thresholding (TwIST) framework [22], a modified and fast version of standard iterative shrinkage/thresholding. Apart from using the wavelet-DCT basis, one can learn a dictionary with which the image cubes can be sparsely represented [13, 23]. An interesting idea to improve the reconstruction quality of the dictionary learning based approach is to use a standard image with red, green, and blue (RGB) components of the same scene as side information [13]. That is, a coupled dictionary is learned from the joint datasets of the CASSI measurements and the corresponding RGB image. We note in passing that using color sensitive RGB detectors directly as the FPA of CASSI is another way to improve the sensing of spectral images, because spatio-spectral coding can be attained in a single snapshot without requiring extra optical elements [24].

Despite the good results attained with the algorithms mentioned above, they all need manual tuning of some parameters, which may be time consuming. In GPSR and TwIST, the optimal regularization parameter could be different in reconstructing different image cubes; in dictionary learning methods, the patch size and the number of dictionary atoms need to be chosen carefully.

C. Contributions

In this paper, we develop a robust and fast reconstruction algorithm for the CASSI system using approximate message passing (AMP) [18]. AMP is an iterative algorithm that can apply image denoising at each iteration. Previously, we proposed a 2D compressive imaging reconstruction algorithm, AMP-Wiener [25], where an adaptive Wiener filter was applied as the image denoiser within AMP. Our numerical results showed that AMP-Wiener outperformed prior art algorithms in term of both reconstruction quality and runtime. In this paper, AMP-Wiener is extended to reconstruct 3D hyperspectral images. Because the matrix that models the CASSI system is highly sparse, structured, and ill-conditioned, applying AMP to the CASSI system becomes challenging. For example, (i) the noisy image cube that is obtained at each AMP iteration contains non-Gaussian noise; and (ii) AMP encounters divergence problems, i.e., the reconstruction error may increase with more iterations. In order to overcome these challenges, we modify the adaptive Wiener filter to fit the 3D image denoising problem, and use damping [26, 27], which resembles a technique used in Gaussian belief propagation [28], to encourage the convergence of AMP.

We simulate our algorithm on several different settings, and the numerical results show that AMP-Wiener reconstructs 3D image cubes with less runtime and higher quality than other compressive hyperspectral imaging reconstruction algorithms such as GPSR [19] and TwIST [15, 22] (Figure 3), even when the regularization parameters in GPSR and TwIST have already been tuned. These favorable results provide AMP-Wiener major advantages over GPSR and TwIST. First, when the bottleneck is the time required to run the reconstruction algorithm, AMP-Wiener can provide the same reconstruction quality in 100 seconds that the other algorithms provide in 450 seconds (Figure 3). Second, when the bottleneck is the time required for signal acquisition by CASSI hardware, the improved reconstruction quality could allow to reduce the number of shots taken by CASSI by as much as a factor of 2

(Figure 8). Finally, the reconstructed image cube can be obtained by running AMP-Wiener only once, because AMP-Wiener does not need to tune any parameters. In contrast, the regularization parameters in GPSR and TwIST need to be tuned carefully. The optimal values of these parameters may vary for different test image cubes. In order to tune the parameters for each test image cube, we run GPSR and TwIST many times with different parameter values, and then select the ones that provide the best results.

The remainder of the paper is arranged as follows. We review CASSI in Section II, and describe our AMP based compressive hyperspectral imaging reconstruction algorithm in Section III. Numerical results are presented in Section IV, while Section V concludes.

II. Coded Aperture Snapshot Spectral Imager (CASSI)

A. Mathematical representation of CASSI

The coded aperture snapshot spectral imager (CASSI) [17] is a compressive spectral imaging system that collects far fewer measurements than traditional spectrometers. In CASSI, (i) the 2D spatial information of a scene is coded by an aperture, (ii) the coded spatial projections are spectrally shifted by a dispersive element, and (iii) the coded and shifted projections are detected by a 2D FPA. That is, in each coordinate of the FPA, the received projection is an integration of the coded and shifted voxels over all spectral bands at the same spatial coordinate. More specifically, let $f_0(x, y, \lambda)$ denote the density of a scene at spatial coordinate (x, y) and at wavelength λ, and let $T(x, y)$ denote the coded aperture. The coded density $T(x, y)f_0(x, y, \lambda)$ is then spectrally shifted by the dispersive element along one of the spatial dimensions. The energy received by the FPA at coordinate (x, y) is therefore

$$g(x, y) = \int_{\Lambda} T(x, y - S(\lambda))f_0(x, y - S(\lambda), \lambda)d\lambda, \tag{1}$$

where $S(\lambda)$ is the dispersion function induced by the prism at wavelength λ. Suppose we take a scene of spatial dimension M by N and spectral dimension L, i.e., the dimension of the image cube is $M \times N \times L$, and the dispersion is along the second spatial dimension y, then the number of measurements captured by the FPA will be $M(N + L - 1)$. If we approximate the integral in (1) by a discrete summation and vectorize the 3D image cube and the 2D measurements, then we obtain a matrix-vector form of (1),

$$\mathbf{g} = \mathbf{H}\mathbf{f_0} + \mathbf{z}, \tag{2}$$

where $\mathbf{f_0}$ is the vectorized 3D image cube of dimension $n = MNL$, vectors $\mathbf{g}$ and $\mathbf{z}$ are the measurements and the additive noise, respectively, and the matrix $\mathbf{H}$ is an equivalent linear operator that models the integral in (1). With a single shot of CASSI, the number of measurements is $m = M(N + L - 1)$, whereas K shots will yield $m = KM(N + L - 1)$ measurements. The matrix H in (2) accounts for the effects of the coded aperture and the dispersive element. A sketch of this matrix is depicted in Figure 1(a) when $K = 2$ shots are used. It consists of a set of diagonal patterns that repeat in the horizontal direction, each time with a unit downward shift, as many times as the number of spectral bands. Each diagonal pattern is the coded aperture itself after being column-wise vectorized. Just below, the next set of diagonal patterns are determined by the coded aperture pattern used in the subsequent shot. The matrix H will thus have as many sets of diagonal patterns as FPA measurements.

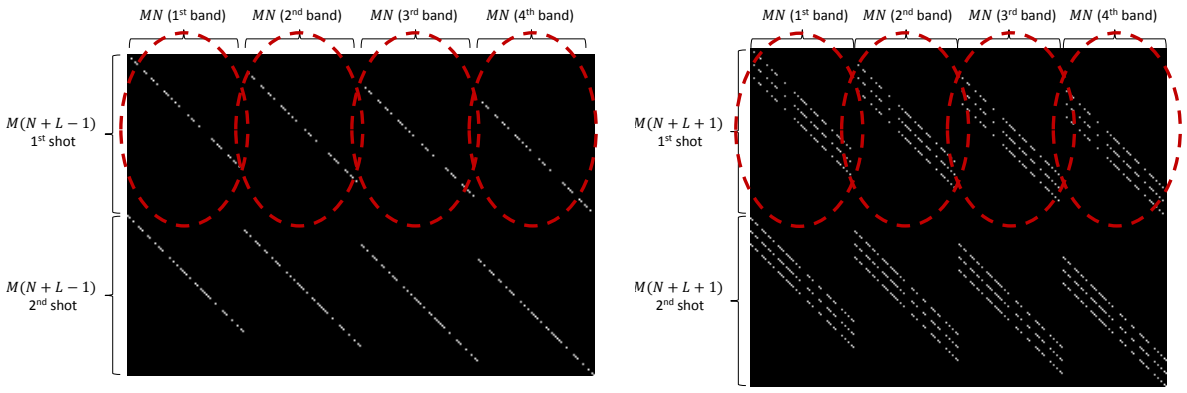

(a) The matrix $\mathbf{H}$ for standard CASSI

(b) The matrix $\mathbf{H}$ for higher order CASSI

Figure 1: *The matrix* $\mathbf{H}$ *is presented for* $K = 2, M = N = 8, L = 4$*. The circled diagonal patterns that repeat horizontally correspond to the coded aperture pattern used in the first FPA shot. The second coded aperture pattern determines the next set of diagonals. In (a) standard CASSI, each FPA shot captures* $M(N + L - 1) = 88$ *measurements; in (b) higher order CASSI, each FPA shot captures* $M(N + L + 1) = 104$ *measurements.*

B. Higher order CASSI

Recently, Arguello et al. [29] proposed a higher order model to characterize the CASSI system with greater precision, and improved the quality of the reconstructed 3D image cubes. In the standard CASSI system model, each cubic voxel in the 3D cube contributes to exactly one measurement in the FPA. In the higher order CASSI model, however, each cubic voxel is shifted to an oblique voxel because of the continuous nature of the dispersion, and therefore the oblique voxel contributes to more than one measurement in the FPA. As a result, the matrix $\mathbf{H}$ in (2) will have multiple diagonals as shown in Figure 1(b), where there are sets of 3 diagonals for each FPA shot, accounting for the voxel energy impinging into the neighboring FPA pixels. In this case, the number of measurements with $K = 1$ shot of CASSI will be $m = M(N + L + 1)$, because each diagonal entails the use of M more pixels (we refer readers to [29] for details).

In Section IV, we will provide promising image reconstruction results for this higher order CASSI system. Using the standard CASSI model, our proposed algorithm produces similar advantageous results over other competing algorithms.

III. Proposed Algorithm

The goal of our proposed algorithm is to reconstruct the image cube $\mathbf{f_0}$ from its compressive measurements $\mathbf{g}$, where the matrix $\mathbf{H}$ is known. In this section, we describe our algorithm in detail. The algorithm employs (i) approximate message passing (AMP) [18], an iterative algorithm for compressive sensing problems, and (ii) adaptive Wiener filtering, a hyperspectral image denoiser that can be applied within each iteration of AMP.

A. Image denoising in scalar channels

Below we describe that the linear imaging system model in (2) can be converted to a 3D image denoising problem in scalar channels. Therefore, we begin by defining scalar channels, where the noisy observations $\mathbf{q}$ of the image cube $\mathbf{f_0}$ obey

$$\mathbf{q} = \mathbf{f_0} + \mathbf{v}, \tag{3}$$

and $\mathbf{v}$ is the additive noise vector. Recovering $\mathbf{f_0}$ from $\mathbf{q}$ is known as a 3D image denoising problem.

B. Approximate message passing

AMP [18] has recently become a popular algorithm for solving signal reconstruction problems in linear systems as defined in (2). The AMP algorithm proceeds iteratively according to

$$\mathbf{f}^{t+1} = \eta_t(\mathbf{H}^T\mathbf{r}^t + \mathbf{f}^t), \tag{4}$$

$$\mathbf{r}^t = \mathbf{g} - \mathbf{H}\mathbf{f}^t + \frac{1}{R}\mathbf{r}^{t-1}\langle \eta'_{t-1}(\mathbf{H}^T\mathbf{r}^{t-1} + \mathbf{f}^{t-1})\rangle, \tag{5}$$

where $\mathbf{H}^T$ is the transpose of $\mathbf{H}$, $R = m/n$ represents the measurement rate, $\eta_t(\cdot)$ is a denoising function at the t-th iteration, $\eta'_t(\mathbf{s}) = \frac{\partial}{\partial \mathbf{s}}\eta_t(\mathbf{s})$, and $\langle \mathbf{u}\rangle = \frac{1}{n}\sum_{i=1}^{n} u_i$ for some vector $\mathbf{u} = (u_1, u_2, \ldots, u_n)$. We will explain in Section III-E how $\mathbf{f}^t$ and $\mathbf{r}^t$ are initialized. The last term in (5) is called the "Onsager reaction term" [18, 30] in statistical physics, and this Onsager reaction term helps improve the phase transition (trade-off between the measurement rate and signal sparsity) of the reconstruction process. In the t-th iteration, we obtain the vectors $\mathbf{f}^t$ and $\mathbf{r}^t$. We highlight that the vector $\mathbf{H}^T\mathbf{r}^t + \mathbf{f}^t$ in (4) can be regarded as a noise-corrupted version of $\mathbf{f_0}$ in the t-th iteration with noise variance σ_t^2, and therefore $\eta_t(\cdot)$ is a 3D image denoising function that is performed on a scalar channel as in (3). Let us denote the equivalent scalar channel at iteration t by

$$\mathbf{q}^t = \mathbf{H}^T\mathbf{r}^t + \mathbf{f}^t = \mathbf{f_0} + \mathbf{v}^t, \tag{6}$$

where the noise level σ_t^2 is estimated by [31],

$$\widehat{\sigma}_t^2 = \frac{1}{m}\sum_{i=1}^{m}(r_i^t)^2, \tag{7}$$

and r_i^t denotes the i-th component of the vector $\mathbf{r}^t$ in (5).

C. Adaptive Wiener filter

We are now ready to describe our 3D image denoiser, which is the function $\eta_t(\cdot)$ in the first step of AMP iterations in (4). Recall that in 2D image denoising problems, a 2D wavelet transform is often performed and some shrinkage function is applied to the wavelet coefficients in order to suppress noise [32, 33]. The wavelet transform based image denoising method is effective, because natural images are usually sparse in the wavelet transform domain, i.e., there are only a few large wavelet coefficients and the rest of the coefficients are small. Therefore, large wavelet coefficients are likely to contain information about the image, whereas small coefficients are usually comprised mostly of noise, and so it is effective to denoise by shrinking the small coefficients toward zero and

suppressing the large coefficients according to the noise variance. Similarly, in hyperspectral image denoising, we want to find a sparsifying transform such that hyperspectral images have only a few large coefficients in this transform domain. Inspired by Arguello and Arce [34], we apply a wavelet transform to each of the 2D images in a 3D cube, and then apply a discrete cosine transform (DCT) along the spectral dimension, because the 2D slices from different wavelengths are highly correlated. That is, the sparsifying transform $\mathbf{\Psi}$ can be expressed as a Kronecker product of a DCT transform $\mathbf{\Phi}$ and a 2D wavelet transform $\mathbf{W}$, i.e., $\mathbf{\Psi} = \mathbf{\Phi} \otimes \mathbf{W}$, and it can easily be shown that $\mathbf{\Psi}$ is an orthonormal transform. Our 3D image denoising is processed after applying the sparsifying transform $\mathbf{\Psi}$ to the noisy image cube $\mathbf{q}^t$.

In our previous work [25] on compressive imaging reconstruction problems for 2D images, one of the image denoisers we employed was an adaptive Wiener filter in the wavelet domain, where the variance of each wavelet coefficient was estimated from its neighboring coefficients within a 5×5 window, i.e., the variance was estimated locally. Such an image denoiser performed well in the 2D compressive imaging problem, because the scalar channel (6) obtained from the AMP iterations (4,5) was an additive white Gaussian noise channel, and each wavelet coefficient contained independent and identically distributed (i.i.d.) Gaussian noise. In the CASSI system (2), however, because the matrix $\mathbf{H}$ is ill-conditioned as shown in Figure 1, the scalar channel (6) that is produced by AMP iterations is not additive white Gaussian, and the noisy 3D image cube $\mathbf{q}^t$ contains non-i.i.d. Gaussian noise. Consequently, estimating the coefficient variance from its small neighboring coefficients (a 3×3 or 5×5 neighboring window) may not be accurate. Therefore, we modify the local variance estimation to a global estimation within each wavelet subband, and our simulation results show that global estimation provides better reconstruction quality than local estimation for hyperspectral images. Specifically, let $\theta^t_{\mathbf{q}}$ denote the coefficients of $\mathbf{q}^t$ in the transform domain, i.e., $\theta^t_{\mathbf{q}} = \mathbf{\Psi}\mathbf{q}$, and $\theta^t_{\mathbf{q},i}$ is the i-th element of $\theta^t_{\mathbf{q}}$. The coefficients $\widehat{\theta}^t_{\mathbf{f}}$ of the estimated (denoised) image cube $\mathbf{f}^t$ are obtained by Wiener filtering,

$$\widehat{\theta}^t_{\mathbf{f},i} = \frac{\max\{0, \widehat{\sigma}^2_{i,t} - \sigma^2_t\}}{(\widehat{\sigma}^2_{i,t} - \sigma^2_t) + \sigma^2_t} \left(\theta^t_{\mathbf{q},i} - \widehat{\mu}_{i,t}\right) + \widehat{\mu}_{i,t} = \frac{\max\{0, \widehat{\sigma}^2_{i,t} - \sigma^2_t\}}{\widehat{\sigma}^2_{i,t}} \left(\theta^t_{\mathbf{q},i} - \widehat{\mu}_{i,t}\right) + \widehat{\mu}_{i,t}, \tag{8}$$

where $\widehat{\mu}_{i,t}$ and $\widehat{\sigma}^2_{i,t}$ are the empirical mean and variance of $\theta^t_{\mathbf{q},i}$ within an appropriate wavelet subband, respectively. Taking the maximum between 0 and $(\widehat{\sigma}^2_{i,t} - \sigma^2_t)$ ensures that if the empirical variance $\widehat{\sigma}^2_{i,t}$ of the noisy coefficients is smaller than the noise variance σ^2_t, then the corresponding noisy coefficients are set to 0. After obtaining the denoised coefficients $\widehat{\theta}^t_{\mathbf{f}}$, the estimated image cube in the t-th iteration satisfies $\mathbf{f}^t = \mathbf{\Psi}^{-1}\widehat{\theta}^t_{\mathbf{f}} = \mathbf{\Psi}^T\widehat{\theta}^t_{\mathbf{f}}$.

D. Derivative of adaptive Wiener filter

The adaptive Wiener filter described in Section III-C is applied in (4) as the 3D image denoising function $\eta_t(\cdot)$. The following step in (5) requires $\eta'_t(\cdot)$, i.e., the derivative of $\eta_t(\cdot)$. We now show how to obtain $\eta'_t(\cdot)$. It has been discussed [25] that when the sparsifying transform is orthonormal, the derivative calculated in the transform domain is equivalent to the derivative in the image domain. According to (8), the derivative of the Wiener filter in the transform domain with respect to $\widehat{\theta}^t_{\mathbf{q},i}$ is $\max\{0, \widehat{\sigma}^2_{i,t} - \sigma^2_t\}/\widehat{\sigma}^2_{i,t}$. Because the sparsifying transform $\mathbf{\Psi}$ is

orthonormal, the Onsager term in (5) can be calculated efficiently as

$$\langle \eta_t'(\mathbf{H}^T\mathbf{r}^t + \mathbf{f}^t)\rangle = \frac{1}{n}\sum_{i\in\mathcal{I}} \frac{\max\{0, \widehat{\sigma}_{i,t}^2 - \sigma_t^2\}}{\widehat{\sigma}_{i,t}^2}, \tag{9}$$

where $\mathcal{I}$ is the index set of all image cube elements, and the cardinality of $\mathcal{I}$ is $n = MNL$.

We focus on image denoising in an orthonormal transform domain and apply Wiener filtering to suppress noise, because it is convenient to obtain the Onsager correction term in (5). On the other hand, other denoisers that are not wavelet-DCT based can also be applied within the AMP framework. Metzler et al. [35], for example, proposed to utilize a block matching and 3D filtering denoising scheme (BM3D) [36] within AMP for 2D compressive imaging reconstruction, and run Monte Carlo [37] to estimate the Onsager correction term. However, the Monte Carlo technique is accurate only when the scalar channel (6) is Gaussian. In the CASSI system model (2), BM4D [38] may be an option for the 3D image denoising procedure. However, because the matrix $\mathbf{H}$ is ill-conditioned, the scalar channel (6) that is produced by AMP iterations (4,5) is not Gaussian, and thus the Monte Carlo technique fails to estimate the Onsager correction term.

E. AMP-Wiener

Basic AMP has been proved to converge with i.i.d. Gaussian matrices [39]. Other AMP variants [26, 40, 41] have been proposed in order to encourage convergence for a broader class of measurement matrices. The matrix $\mathbf{H}$ defined in (2) is not i.i.d. Gaussian, but highly structured as shown in Figure 1. Unfortunately, AMP-Wiener encounters divergence issues with this matrix $\mathbf{H}$. The divergence issues of AMP-Wiener can be detected by evaluating the value of $\widehat{\sigma}_t^2$ obtained by (7) as a function of iteration number t. Recall that $\widehat{\sigma}_t^2$ estimates the amount of noise in the noisy image cube $\mathbf{q}^t$ at iteration t. If AMP-Wiener converges, then we expect the value of $\widehat{\sigma}_t^2$ to decrease as t increases. Otherwise, we know that AMP-Wiener diverges. We choose to apply "damping" [26, 27] to solve for the divergence problems of AMP-Wiener, because it is simple and only increases the runtime modestly. Specifically, damping is an extra step within AMP iterations. In (4), instead of updating the value of $\mathbf{f}^{t+1}$ by the output of the denoiser $\eta_t(\mathbf{H}^T\mathbf{r}^t + \mathbf{f}^t)$, we assign a weighted average of $\eta_t(\mathbf{H}^T\mathbf{r}^t + \mathbf{f}^t)$ and $\mathbf{f}^t$ to $\mathbf{f}^{t+1}$ as follows,

$$\mathbf{f}^{t+1} = \alpha \cdot \eta_t(\mathbf{H}^T\mathbf{r}^t + \mathbf{f}^t) + (1-\alpha)\cdot \mathbf{f}^t, \tag{10}$$

for some constant $0 < \alpha \leq 1$. Similarly, after obtaining $\mathbf{r}^t$ in (5), we add an extra damping step,

$$\mathbf{r}^t = \alpha \cdot \mathbf{r}^t + (1-\alpha)\cdot \mathbf{r}^{t-1}, \tag{11}$$

with the same value of α as that in (10).

Our proposed AMP-Wiener is summarized in Algorithm 1, where $\widehat{\mathbf{f}}_{\text{AMP}}$ denotes the image cube reconstructed by AMP-Wiener. Note that in the first iteration of Algorithm 1, initialization of $\mathbf{q}^0$ and $\widehat{\sigma}_0^2$ may not be necessary, because $\mathbf{r}^0$ is an all-zero vector, and the Onsager term is 0 at iteration 1.

Algorithm 1 AMP-Wiener

Inputs: $\mathbf{g}$, $\mathbf{H}$, α, maxIter

Outputs: $\widehat{\mathbf{f}}_{\text{AMP}}$

Initialization: $\mathbf{f}^1 = \mathbf{0}$, $\mathbf{r}^0 = \mathbf{0}$

for $t = 1$: maxIter **do**

1) $\mathbf{r}^t = \mathbf{g} - \mathbf{H}\mathbf{f}^t + \frac{1}{R}\mathbf{r}^{t-1}\frac{1}{n}\sum_{i=1}^{n}\frac{\max\{0,\widehat{\sigma}^2_{i,t-1}-\sigma^2_{t-1}\}}{\widehat{\sigma}^2_{i,t-1}}$
2) $\mathbf{r}^t = \alpha \cdot \mathbf{r}^t + (1-\alpha)\cdot \mathbf{r}^{t-1}$
3) $\mathbf{q}^t = \mathbf{H}^T\mathbf{r}^t + \mathbf{f}^t$
4) $\widehat{\sigma}^2_t = \frac{1}{m}\sum_j (r^t_j)^2$
5) $\theta^t_{\mathbf{q}} = \mathbf{\Psi}\mathbf{q}^t$
6) $\widehat{\theta}^t_{\mathbf{f},i} = \frac{\max\{0,\widehat{\sigma}^2_{i,t}-\sigma^2_t\}}{\widehat{\sigma}^2_{i,t}}\left(\theta^t_{\mathbf{q},i} - \widehat{\mu}_{i,t}\right) + \widehat{\mu}_{i,t}$
7) $\mathbf{f}^{t+1} = \alpha \cdot \mathbf{\Psi}^T\widehat{\theta}^t_{\mathbf{f}} + (1-\alpha)\cdot \mathbf{f}^t$

end for

$\widehat{\mathbf{f}}_{\text{AMP}} = \mathbf{f}^{\text{maxIter+1}}$

IV. Numerical Results

In this section, we provide numerical results where we compare the reconstruction quality and runtime of AMP-Wiener, gradient projection for sparse reconstruction (GPSR) [19], and two-step iterative shrinkage/thresholding (TwIST) [15, 22]. In all experiments, we use the same coded aperture pattern for AMP-Wiener, GPSR, and TwIST. In order to quantify the reconstruction quality of each algorithm, the peak signal to noise ratio (PSNR) of each 2D slice in reconstructed cubes is measured. The PSNR is defined as the ratio between the maximum squared value of the ground truth image cube $\mathbf{f_0}$ and the mean square error of the estimation $\widehat{\mathbf{f}}$, i.e.,

$$\text{PSNR} = 10 \cdot \log_{10}\left(\frac{\max_{x,y,\lambda}\left(f^2_{0,(x,y,\lambda)}\right)}{\sum_{x,y,\lambda}\left(\widehat{f}_{(x,y,\lambda)} - f_{0,(x,y,\lambda)}\right)^2}\right),$$

where $f_{(x,y,\lambda)}$ denotes the element in the cube $\mathbf{f}$ at spatial coordinate (x, y) and spectral coordinate λ.

In AMP, the damping parameter α is set to be 0.2. Other damping values are possible, but for smaller values such as 0.1, the reconstruction quality improves more slowly as the iteration number increases; for larger values such as 0.5, AMP may diverge. Recall that the amount of damping can be adjusted by evaluating the values of $\widehat{\sigma}^2_t$ from (7). The choice of damping mainly depends on the structure of the imaging model in (2) but not on the characteristics of the image cubes, and thus the value of the damping parameter α need not be tuned in our experiments.

To reconstruct the image cube $\mathbf{f_0}$, GPSR and TwIST minimize objective functions of the form

$$\widehat{\mathbf{f}} = \arg\min_{\mathbf{f}} \frac{1}{2}\|\mathbf{g} - \mathbf{H}\mathbf{f}\|_2^2 + \beta \cdot \phi(\mathbf{f}), \tag{12}$$

where $\phi(\cdot)$ is a regularization function that characterizes the structure of the image cube $\mathbf{f_0}$, and β is a regularization parameter that balances the weights of the two terms in the objective function. In GPSR, $\phi(\mathbf{f}) = \|\mathbf{\Psi}\mathbf{f}\|_1$; in TwIST,

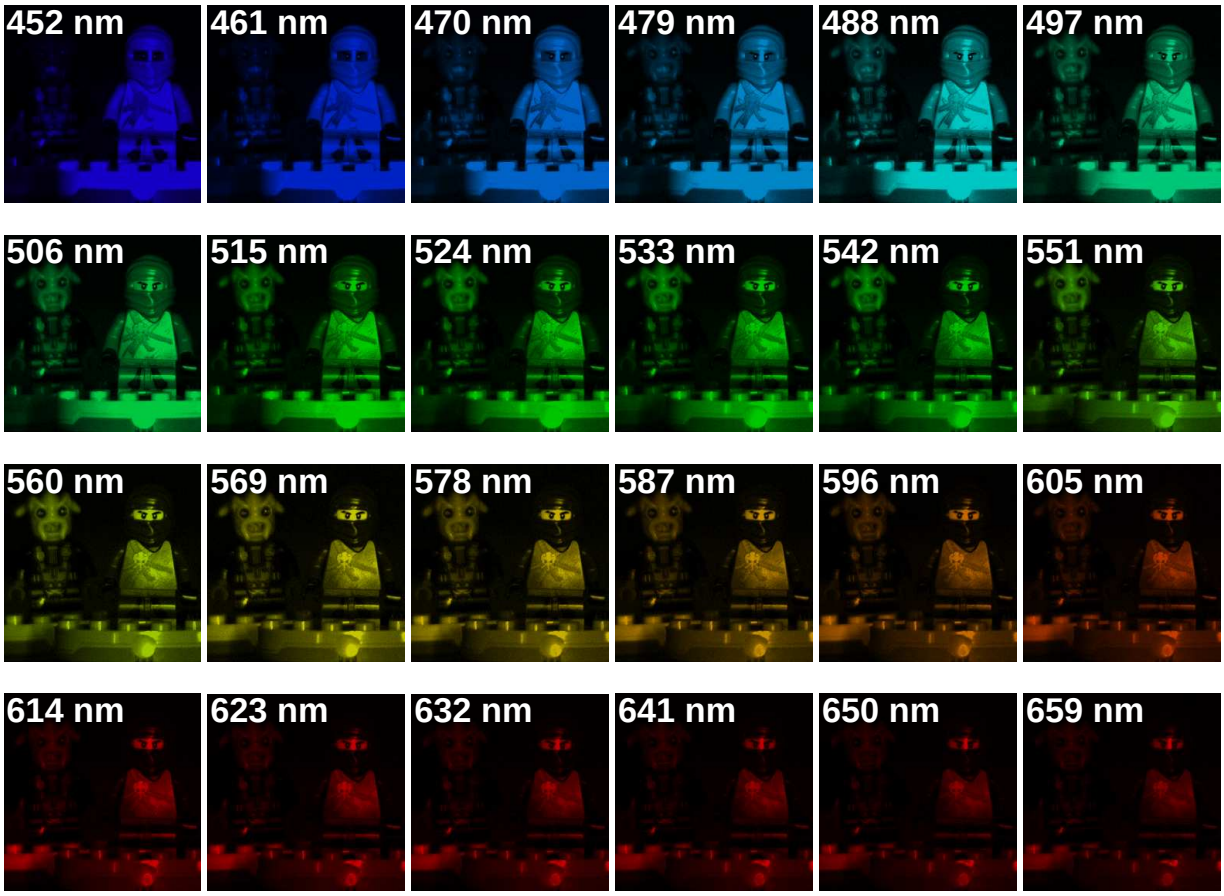

Figure 2: *The scene of Lego. (The target object presented in the experimental results was not endorsed by the trademark owners and it is used here as fair use to illustrate the quality of reconstruction of compressive spectral image measurements. LEGO is a trademark of the LEGO Group, which does not sponsor, authorize or endorse the images in this paper. The LEGO Group. All Rights Reserved. http://aboutus.lego.com/en-us/legal-notice/fair-play/.)*

the total variation regularizer is employed,

$$\phi(\mathbf{f}) = \sum_{\lambda=1}^{L}\sum_{x=1}^{M}\sum_{y=1}^{N}\left((f(x+1,y,\lambda)-f(x,y,\lambda))^2+(f(x,y+1,\lambda)-f(x,y,\lambda))^2\right)^{1/2}. \tag{13}$$

The value of the regularization parameter β in (12) greatly affects the reconstruction results of GPSR and TwIST, and must be tuned carefully. We select the optimal values of β for GPSR and TwIST manually, i.e., we run GPSR and TwIST with $5-10$ different values of β, and select the results with the highest PSNR. The typical value of regularization parameter for GPSR is between 10^{-5} and 10^{-4}, and the value for TwIST is around 0.1. We note in passing that the ground truth image cube is not known in practice, and estimating the PSNR obtained using different β may be quite involved and require oracle-like information when using GPSR and TwIST. There exist other hyperspectral image reconstruction algorithms based on dictionary learning [13, 23]. However, it is

not straightforward to modify these dictionary learning methods to the higher order CASSI model described in Section II-B, and so we do not include these algorithms in the comparison.

A. Test on "Lego" image cube

The first set of simulations is done using a cube of the scene shown as Figure 2. This data cube was acquired using a wide-band Xenon lamp as the illumination source, modulated by a visible monochromator spanning the spectral range between 448 nm and 664 nm, and each waveband has 9 nm width. The image intensity was captured using a grayscale CCD camera, with pixel size 9.9 μm, and 8 bits of intensity levels. The resulting test data cube has $M \times N = 256 \times 256$ pixels of spatial resolution and $L = 24$ spectral bands.

Setting 1: The measurements $\mathbf{g}$ are captured with $K = 2$ shots such that the coded aperture in the second shot is the complement of the aperture in the first shot. Therefore, we ensure that in the matrix $\mathbf{H}$ in (2), the norm of each column is similar. The measurement rate with two shots is $m/n = KM(N + L + 1)/(MNL) \approx 0.09$. Moreover, we add Gaussian noise with zero mean to the measurements. The signal to noise ratio (SNR) is defined as $10 \log_{10}(\mu_g/\sigma_{\text{noise}})$ [34], where μ_g is the mean value of the measurements $\mathbf{Hf_0}$ and σ_{noise} is the standard deviation of the additive noise $\mathbf{z}$. In Setting 1, we add measurement noise such that the SNR is 20 dB.

Figure 3 compares the reconstruction quality of AMP-Wiener, GPSR, and TwIST within a certain amount of runtime. Runtime is measured on a Dell OPTIPLEX 9010 running an Intel(R) CoreTM i7-860 with 16GB RAM, and the environment is Matlab R2013a. In Figure 3, the horizontal axis represents runtime in seconds, and the vertical axis is the averaged PSNR over the 24 spectral bands. Although the PSNR of AMP-Wiener oscillates at the first few iterations, which may be because the matrix $\mathbf{H}$ is ill-conditioned, it becomes stable after 50 seconds and reaches a higher level when compared to the PSNRs of GPSR and TwIST at 50 seconds. After 450 seconds, the average PSNR of the cube reconstructed by AMP-Wiener (solid curve with triangle markers) is 26.16 dB, while the average PSNRs of GPSR (dash curve with circle markers) and TwIST (dash-dotted curve with cross markers) are 23.46 dB and 25.10 dB, respectively. Note that in 450 seconds, TwIST runs around 200 iterations, while AMP-Wiener and GPSR run 400 iterations.

Figure 4 complements Figure 3 by illustrating the PSNR of each 2D slice in the reconstructed cube separately. It is shown that the cube reconstructed by AMP-Wiener has $2 - 4$ dB higher PSNR than the cubes by GPSR and $0.4 - 3$ dB higher than that of TwIST for all 24 slices.

In Figure 5, we plot the 2D slices at wavelengths 488 nm, 533 nm, and 578 nm in the actual image cubes reconstructed by AMP-Wiener, GPSR, and TwIST. The images in these four rows are slices from the ground truth image cube $\mathbf{f_0}$, the cubes reconstructed by AMP-Wiener, GPSR, and TwIST, respectively. At the same time, the images in columns $1 - 3$ show the upper-left part of the scene, whereas images in columns $4 - 6$ show the upper-right part of the scene. All images are of size 128×128. It is clear from Figure 5 that the 2D slices reconstructed by AMP-Wiener have better visual quality; the slices reconstructed by GPSR have blurry edges, and the slices reconstructed by TwIST lack details because the total variation regularization tends to constrain the images to be piecewise constant.

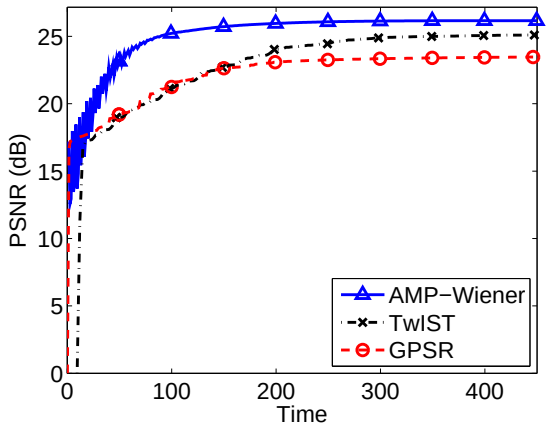

Figure 3: *Runtime versus average PSNR comparison of AMP-Wiener, GPSR, and TwIST for the Lego image cube. Cube size is* $M = N = 256$*, and* $L = 24$*. The measurements are captured with* $K = 2$ *shots using complementary coded apertures, and the number of measurements is* $m = 143,872$*. Random Gaussian noise is added to the measurements such that the SNR is 20 dB.*

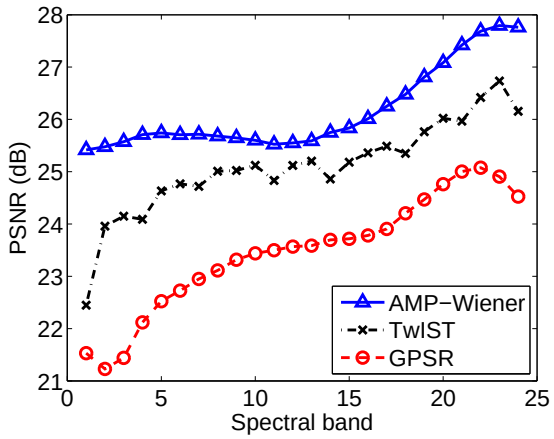

Figure 4: *Spectral band versus PSNR comparison of AMP-Wiener, GPSR, and TwIST for the Lego image cube. Cube size is* $M = N = 256$*, and* $L = 24$*. The measurements are captured with* $K = 2$ *shots using complementary coded apertures, and the number of measurements is* $m = 143,872$*. Random Gaussian noise is added to the measurements such that the SNR is 20 dB.*

Furthermore, a spectral signature plot analyzes how the pixel values change along the spectral dimension at a fixed spatial location, and we present such spectral signature plots for the image cubes reconstructed by AMP-Wiener, GPSR, and TwIST in Figure 6. Three spatial locations are selected as shown in Figure 6(a), and the spectral signature plots for locations B, C, and D are shown in Figures 6(b)–6(d), respectively. It can be seen that the spectral signatures of the cube reconstructed by AMP-Wiener closely resemble those of the ground truth image cube (dotted curve with square markers), whereas there are obvious discrepancies between the spectral signatures of the cube reconstructed by GPSR or TwIST and those of the ground truth cube.

According to the runtime experiment from Setting 1, we run AMP-Wiener with 400 iterations, GPSR with 400

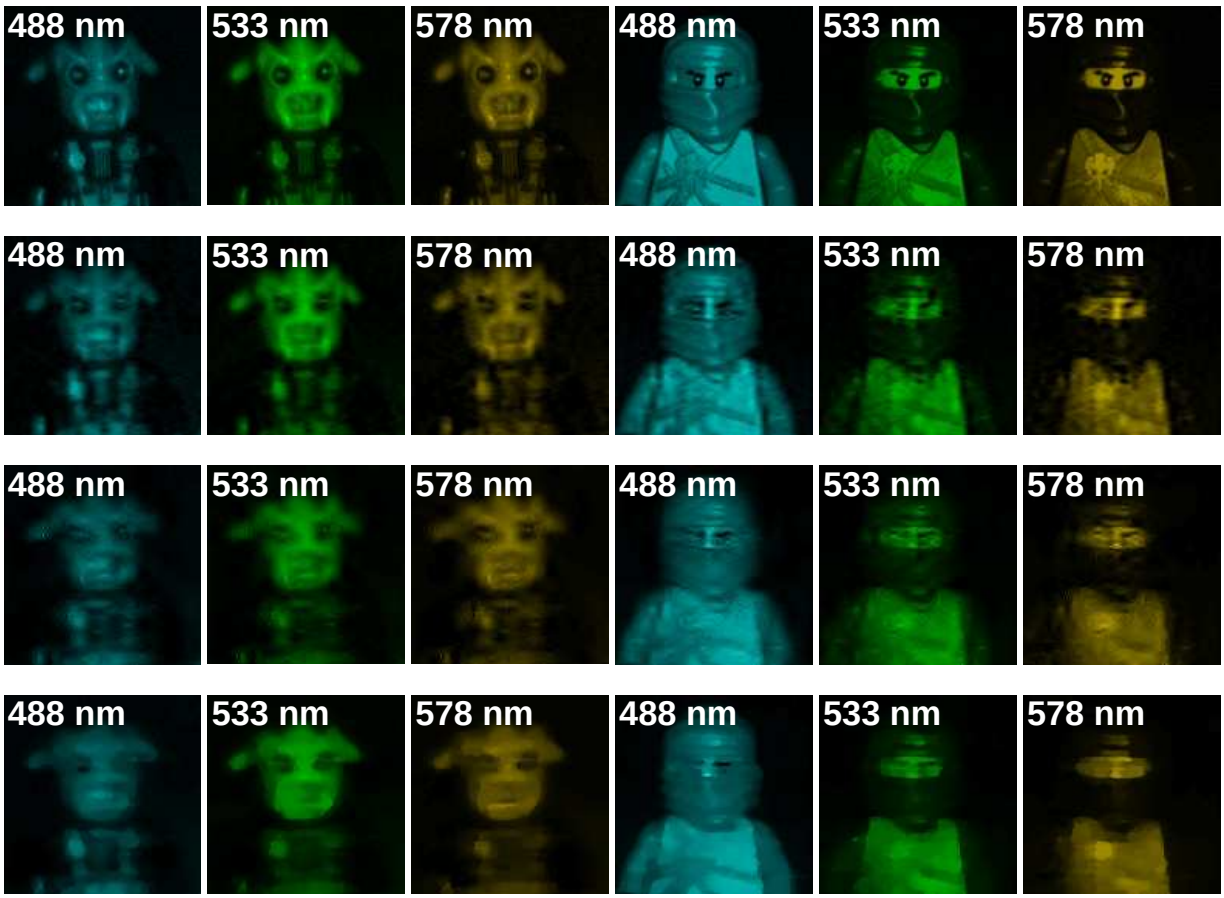

Figure 5: *2D slices at wavelengths* 488 *nm,* 533 *nm, and* 578 *nm in the image cubes reconstructed by AMP-Wiener, GPSR, and TwIST for the Lego image cube. Cube size is* $M = N = 256$*, and* $L = 24$*. The measurements are captured with* $K = 2$ *shots using complementary coded apertures, and the number of measurements is* $m = 143,872$*. Random Gaussian noise is added to the measurements such that the SNR is 20 dB. First row: ground truth; second row: the reconstruction result by AMP-Wiener; third row: the reconstruction result by GPSR; last row: the reconstruction result by TwIST. Columns* $1-3$*: upper-left part of the scene of size* 128×128*; columns* $4-6$*: upper-right part of the scene of size* 128×128*.*

iterations, and TwIST with 200 iterations for the rest of the simulations, so that all algorithms complete within the same amount of time.

Setting 2: In this experiment, we add measurement noise such that the SNR varies from 15 dB to 40 dB, which is the same setting as in Arguello and Arce [34], and the result is shown in Figure 7. Again, AMP-Wiener achieves more than 2 dB higher PSNR than GPSR, and about 1 dB higher PSNR than TwIST, overall.

Setting 3: In Settings 1 and 2, the measurements are captured with $K = 2$ shots. We now test our algorithm on the setting where the number of shots varies from $K = 2$ to $K = 12$ with pairwise complementary coded apertures. Specifically, we randomly generate the coded aperture for the k-th shot for $k = 1, 3, 5, 7, 9, 11$, and the

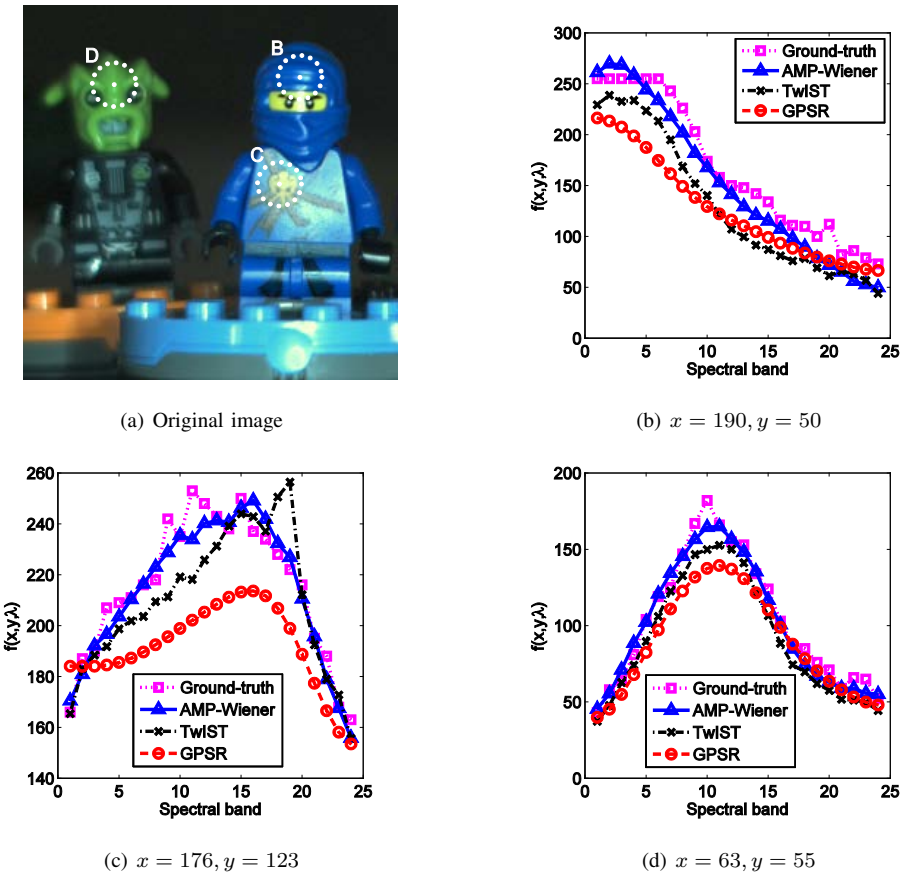

(a) Original image

(b) $x = 190, y = 50$

(c) $x = 176, y = 123$

(d) $x = 63, y = 55$

Figure 6: *Comparison of AMP-Wiener, GPSR, and TwIST on reconstruction along the spectral dimension of three spatial pixel locations as indicated in (a). The estimated pixel values are illustrated for (b) the pixel B, (c) the pixel C, and (d) the pixel D.*

coded aperture in the $(k+1)$-th shot is the complement of the aperture in the k-th shot. In this setting, a moderate amount of noise (20 dB) is added to the measurements. Figure 8 presents the PSNR changes of the reconstructed cubes as the number of shots increases, and AMP-Wiener consistently beats GPSR and TwIST.

B. Test on natural scenes

Besides the Lego image cube, we have also tested our algorithm on image cubes of natural scenes [42].[1] There are two datasets, "natural scenes 2002" and "natural scenes 2004," each one with 8 image data cubes. The cubes in the first dataset have $L = 31$ spectral bands with spatial resolution of around 700×700, whereas the cubes in the second dataset have $L = 33$ spectral bands with spatial resolution of around 1000×1000. To satisfy the dyadic constraint of the 2D wavelet, we crop their spatial resolution to be $M = N = 512$. Because the spatial dimensions

[1]The cubes are downloaded from http://personalpages.manchester.ac.uk/staff/ d.h.foster/Hyperspectral_images_of_natural_scenes_04.html and http://personal pages.manchester.ac.uk/staff/d.h.foster/Hyperspectral_images_of_natural_scenes_02.html.

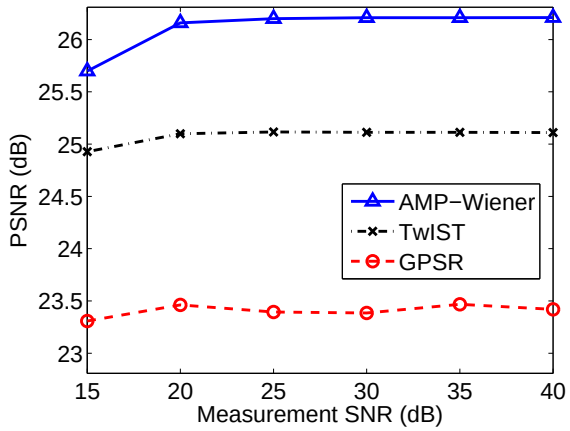

Figure 7: *Measurement noise versus average PSNR comparison of AMP-Wiener, GPSR, and TwIST for the Lego image cube. Cube size is* $M = N = 256$*, and* $L = 24$*. The measurements are captured with* $K = 2$ *shots using complementary coded apertures, and the number of measurements is* $m = 143,872$*.*

of the cubes "scene 6" and "scene7" in the first dataset are smaller than 512×512, we do not include results for these two cubes.

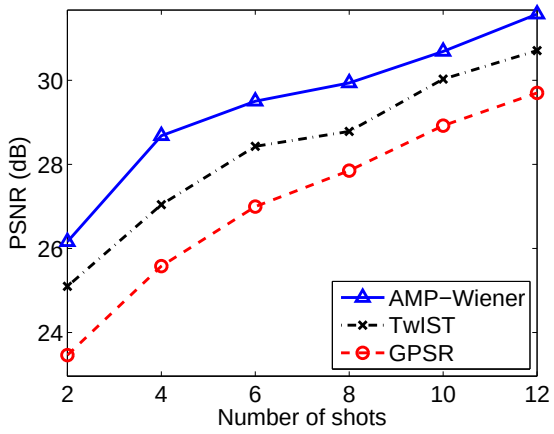

Figure 8: *Number of shots versus average PSNR comparison of AMP-Wiener, GPSR, and TwIST for the Lego image cube. Cube size is* $N = M = 256$*, and* $L = 24$*. The measurements are captured using pairwise complementary coded apertures. Random Gaussian noise is added to the measurements such that the SNR is 20 dB.*

The measurements are captured with $K = 2$ shots, and the measurement rate is $m/n = KM(N + L + 1)/(MNL) \approx 0.069$ for "natural scene 2002" and 0.065 for "natural scene 2004." We test for measurement noise levels such that the SNRs are 15 dB and 20 dB. The typical runtimes for AMP with 400 iterations, GPSR with 400 iterations, and TwIST with 200 iterations are approximately $2,800$ seconds. The average PSNR over all spectral bands for each reconstructed cube is shown in Tables I and II. We highlight the highest PSNR among AMP-Wiener, GPSR, and TwIST using bold fonts. It can be seen from Tables I and II that AMP-Wiener usually

	15 dB			20 dB		
	AMP	GPSR	TwIST	AMP	GPSR	TwIST
Scene 1	**32.69**	28.10	31.05	**33.29**	28.09	31.16
Scene 2	**26.52**	24.32	26.25	**26.65**	24.40	26.41
Scene 3	**32.05**	29.33	31.21	**32.45**	29.55	31.54
Scene 4	**27.57**	25.19	27.17	**27.76**	25.47	27.70
Scene 5	**29.68**	27.09	29.07	**29.80**	27.29	29.42
Scene 8	**28.72**	25.53	26.24	**29.33**	25.77	26.46

TABLE I: *Average PSNR comparison of AMP-Wiener, GPSR, and TwIST for the dataset "natural scene 2002" downloaded from [42]. The spatial dimensions of the cubes are cropped to $M = N = 512$, and each cube has $L = 31$ spectral bands. The measurements are captured with $K = 2$ shots, and the number of measurements is $m = 557,056$. Random Gaussian noise is added to the measurements such that the SNR is 15 or 20 dB. Because the spatial dimensions of the cubes "scene 6" and "scene7" in "natural scenes 2002" are smaller than 512×512, we do not include results for these two cubes.*

	15 dB			20 dB		
	AMP	GPSR	TwIST	AMP	GPSR	TwIST
Scene 1	**30.48**	28.43	30.17	**30.37**	28.53	30.31
Scene 2	**27.34**	24.71	27.03	**27.81**	24.87	27.35
Scene 3	**33.13**	29.38	31.69	**33.12**	29.44	31.75
Scene 4	**32.07**	26.99	31.69	**32.14**	27.25	32.08
Scene 5	**27.44**	24.25	26.48	**27.83**	24.60	26.85
Scene 6	**29.15**	24.99	25.74	**30.00**	25.53	26.15
Scene 7	**36.35**	33.09	33.59	**37.11**	33.55	34.05
Scene 8	**32.12**	28.14	28.22	**32.93**	28.82	28.69

TABLE II: *Average PSNR comparison of AMP-Wiener, GPSR, and TwIST for the dataset "natural scene 2004" downloaded from [42]. The spatial dimensions of the cubes are cropped to $M = N = 512$, and each cube has $L = 33$ spectral bands. The measurements are captured with $K = 2$ shots, and the number of measurements is $m = 559,104$. Random Gaussian noise is added to the measurements such that the SNR is 15 or 20 dB.*

outperforms GPSR by $2 - 5$ dB in terms of the PSNR, and outperforms TwIST by $0.2 - 4$ dB. In addition, the results of 6 selected image cubes are displayed in Figure 9 in the form of 2D RGB images.[2] The four rows of images correspond to ground truth, results by AMP-Wiener, results by GPSR, and results by TwIST, respectively. We can see from Figure 9 that AMP-Wiener produces images with better quality, while images reconstructed by GPSR and TwIST are blurrier.

V. Conclusion

In this paper, we considered the compressive hyperspectral imaging reconstruction problem for the coded aperture snapshot spectral imager (CASSI) system. Considering that the CASSI system is a great improvement in terms of

[2]We refer to the tutorial from http://personalpages.manchester.ac.uk/staff/david.foster/Tutorial_HSI2RGB/Tutorial_HSI2RGB.html and convert 3D image cubes to 2D RGB images.

Figure 9: *Comparison of selected image cubes reconstructed by AMP-Wiener, GPSR, and TwIST for the datasets "natural scene 2002" and "natural scene 2004." The 2D RGB images shown in this figure are converted from their corresponding 3D image cubes. Cube size is* $N = M = 512$*, and* $L = 31$ *for images in columns* $1 - 2$ *or* $L = 33$ *for images in columns* $3 - 6$*. Random Gaussian noise is added to the measurements such that the SNR is 20 dB. First row: ground truth; second row: the reconstruction result by AMP-Wiener; third row: the reconstruction result by GPSR; last row: the reconstruction result by TwIST.*

imaging quality and acquisition speed over conventional spectral imaging techniques, it is desirable to further improve CASSI by accelerating the 3D image cube reconstruction process. Our proposed AMP-Wiener used an adaptive Wiener filter as a 3D image denoiser within the approximate message passing (AMP) [18] framework. AMP-Wiener was faster than existing image cube reconstruction algorithms, and also achieved better reconstruction quality.

In AMP, the derivative of the image denoiser is required, and the adaptive Wiener filter can be expressed in closed form using a simple formula, and so its derivative is easy to compute. Although the matrix that models the CASSI system is ill-conditioned and may cause AMP to diverge, we helped AMP converge using damping, and reconstructed 3D image cubes successfully. Numerical results showed that AMP-Wiener is robust and fast, and outperforms gradient projection for sparse reconstruction (GPSR) and two-step iterative shrinkage/thresholding (TwIST) even when the regularization parameters for GPSR and TwIST are optimally tuned. Moreover, a significant advantage over GPSR and TwIST is that AMP-Wiener need not tune any parameters, and thus an image cube can

be reconstructed by running AMP-Wiener only once, which is critical in real-world scenarios. In contrast, GPSR and TwIST must be run multiple times in order to find the optimal regularization parameters.

Future improvements: In our current AMP-Wiener algorithm for compressive hyperspectral imaging reconstruction, we estimated the noise variance of the noisy image cube within each AMP iteration using (7). In order to denoise the noisy image cube in the sparsifying transform domain, we applied the estimated noise variance value to all wavelet subbands. The noise variance estimation and 3D image denoising method were effective, and helped produce promising reconstruction. However, both the noise variance estimation and the 3D image denoising method may be sub-optimal, because the noisy image cube within each AMP iteration does not contain i.i.d. Gaussian noise, and so the coefficients in the different wavelet subbands may contain different amounts of noise. Therefore, it is possible that the denoising part of the proposed algorithm, including the noise variance estimation, can be further improved. The study of such denoising methods is left for future work.

ACKNOWLEDGMENTS

We thank Sundeep Rangan and Phil Schniter for inspiring discussions on approximate message passing; Lawrance Carin, and Xin Yuan for kind help on numerical experiments; Junan Zhu for informative explanations about CASSI systems; and Nikhil Krishnan for detailed suggestions on the manuscript.

REFERENCES

[1] R. A. Schultz, T. Nielsen, J. R. Zavaleta, R. Ruch, R. Wyatt, and H. R. Garner, "Hyperspectral imaging: A novel approach for microscopic analysis," Cytometry, vol. 43, no. 4, pp. 239–247, Apr. 2001.

[2] S. V. Panasyuk, S. Yang, D. V. Faller, D. Ngo, R. A. Lew, J. E. Freeman, and A. E. Rogers, "Medical hyperspectral imaging to facilitate residual tumor identification during surgery," Cancer Biol. Therapy, vol. 6, no. 3, pp. 439–446, Mar. 2007.

[3] X. Jia and J. A. Richards, "Segmented principal components transformation for efficient hyperspectral remote-sensing image display and classification," IEEE Trans. Geosci. Remote Sens., vol. 37, no. 1, pp. 538–542, Jan. 1999.

[4] F. A. Kruse, J. W. Boardman, and J. F. Huntington, "Comparison of airborne hyperspectral data and eo-1 hyperion for mineral mapping," IEEE Trans. Geosci. Remote Sens., vol. 41, no. 6, pp. 1388–1400, June 2003.

[5] E. K. Hege, D. O'Connell, W. Johnson, S. Basty, and E. L. Dereniak, "Hyperspectral imaging for astronomy and space surviellance," in SPIE's 48th Annu. Meeting Opt. Sci. and Technol., Jan. 2004, pp. 380–391.

[6] D. J. Brady, Optical imaging and spectroscopy. Hoboken, NJ: Wiley, 2009.

[7] M. T. Eismann, Hyperspectral remote sensing. Bellingham, WA: SPIE, 2012.

[8] N. Gat, "Imaging spectroscopy using tunable filters: A review," in Proc. SPIE, vol. 4056, Apr. 2000, pp. 50–64.

[9] D. Donoho, "Compressed sensing," IEEE Trans. Inf. Theory, vol. 52, no. 4, pp. 1289–1306, Apr. 2006.

[10] E. Candès, J. Romberg, and T. Tao, "Robust uncertainty principles: Exact signal reconstruction from highly incomplete frequency information," IEEE Trans. Inf. Theory, vol. 52, no. 2, pp. 489–509, Feb. 2006.

[11] R. G. Baraniuk, "A lecture on compressive sensing," IEEE Signal Process. Mag., vol. 24, no. 4, pp. 118–121, July 2007.

[12] M. Gehm, R. John, D. Brady, R. Willett, and T. Schulz, "Single-shot compressive spectral imaging with a dual-disperser architecture," Opt. Exp., vol. 15, no. 21, pp. 14 013–14 027, Oct. 2007.

[13] X. Yuan, T. Tsai, R. Zhu, P. Llull, D. Brady, and L. Carin, "Compressive hyperspectral imaging with side information," IEEE J. Sel. Topics Signal Process., vol. PP, no. 99, p. 1, Mar. 2015.

[14] Y. August, C. Vachman, Y. Rivenson, and A. Stern, "Compressive hyperspectral imaging by random separable projections in both the spatial and the spectral domains," Appl. Optics, vol. 52, no. 10, pp. D46–D54, Mar. 2013.

[15] A. Wagadarikar, N. Pitsianis, X. Sun, and D. Brady, "Spectral image estimation for coded aperture snapshot spectral imagers," in Proc. SPIE, Sept. 2008, p. 707602.

[16] H. Arguello and G. Arce, "Code aperture optimization for spectrally agile compressive imaging," J. Opt. Soc. Am., vol. 28, no. 11, pp. 2400–2413, Nov. 2011.

[17] A. Wagadarikar, R. John, R. Willett, and D. Brady, "Single disperser design for coded aperture snapshot spectral imaging," Appl. Opt., vol. 47, no. 10, pp. B44–B51, Apr. 2008.

[18] D. L. Donoho, A. Maleki, and A. Montanari, "Message passing algorithms for compressed sensing," Proc. Nat. Academy Sci., vol. 106, no. 45, pp. 18 914–18 919, Nov. 2009.

[19] M. Figueiredo, R. Nowak, and S. J. Wright, "Gradient projection for sparse reconstruction: Application to compressed sensing and other inverse problems," IEEE J. Select. Topics Signal Proces., vol. 1, pp. 586–597, Dec. 2007.

[20] A. Chambolle, "An algorithm for total variation minimization and applications," J. Math. imaging vision, vol. 20, no. 1-2, pp. 89–97, Jan. 2004.

[21] T. Chan, S. Esedoglu, F. Park, and A. Yip, "Recent developments in total variation image restoration," Math. Models Computer Vision, vol. 17, 2005.

[22] J. M. Bioucas-Dias and M. A. Figueiredo, "A new TwIST: Two-step iterative shrinkage/thresholding algorithms for image restoration," IEEE Trans. Image Process., vol. 16, no. 12, pp. 2992–3004, Dec. 2007.

[23] A. Rajwade, D. Kittle, T. Tsai, D. Brady, and L. Carin, "Coded hyperspectral imaging and blind compressive sensing," SIAM J. on Imag. Sci., vol. 6, no. 2, pp. 782–812, Apr. 2013.

[24] H. Rueda, D. Lau, and G. Arce, "Multi-spectral compressive snapshot imaging using RGB image sensors," to appear in Optics Express, 2015.

[25] J. Tan, Y. Ma, and D. Baron, "Compressive imaging via approximate message passing with image denoising," IEEE Trans. Signal Process., vol. 63, no. 8, pp. 2085–2092, Apr. 2015.

[26] S. Rangan, P. Schniter, and A. Fletcher, "On the convergence of approximate message passing with arbitrary matrices," in Proc. IEEE Int. Symp. Inf. Theory (ISIT), July 2014, pp. 236–240.

[27] J. Vila, P. Schniter, S. Rangan, F. Krzakala, and L. Zdeborova, "Adaptive damping and mean removal for the generalized approximate message passing algorithm," ArXiv preprint arXiv:1412.2005, 2014.

[28] J. K. Johnson, D. Bickson, and D. Dolev, "Fixing convergence of Gaussian belief propagation," in Proc. IEEE Int. Symp. Inf. Theory (ISIT), July 2009, pp. 1674–1678.

[29] H. Arguello, H. Rueda, Y. Wu, D. W. Prather, and G. R. Arce, "Higher-order computational model for coded aperture spectral imaging," Appl. Optics, vol. 52, no. 10, pp. D12–D21, Mar. 2013.

[30] D. J. Thouless, P. W. Anderson, and R. G. Palmer, "Solution of 'Solvable model of a spin glass'," Philosophical Magazine, vol. 35, pp. 593–601, 1977.

[31] A. Montanari, "Graphical models concepts in compressed sensing," Compressed Sensing: Theory and Applications, pp. 394–438, 2012.

[32] D. L. Donoho and J. Johnstone, "Ideal spatial adaptation by wavelet shrinkage," Biometrika, vol. 81, no. 3, pp. 425–455, Sept. 1994.

[33] M. Figueiredo and R. Nowak, "Wavelet-based image estimation: An empirical Bayes approach using Jeffrey's noninformative prior," IEEE Trans. Image Process., vol. 10, no. 9, pp. 1322–1331, Sept. 2001.

[34] H. Arguello and G. Arce, "Colored coded aperture design by concentration of measure in compressive spectral imaging," IEEE Trans. Image Process., vol. 23, no. 4, pp. 1896–1908, Mar. 2014.

[35] C. Metzler, A. Maleki, and R. G. Baraniuk, "From denoising to compressed sensing," Arxiv preprint arxiv:1406.4175v2, June 2014.

[36] K. Dabov, A. Foi, V. Katkovnik, and K. Egiazarian, "Image denoising by sparse 3-D transform-domain collaborative filtering," IEEE Trans. Image Process., vol. 16, no. 8, pp. 2080–2095, Aug. 2007.

[37] S. Ramani, T. Blu, and M. Unser, "Monte-Carlo SURE: A black-box optimization of regularization parameters for general denoising algorithms," IEEE Trans. Image Process., vol. 17, no. 9, pp. 1540–1554, Sept. 2008.

[38] M. Maggioni, V. Katkovnik, K. Egiazarian, and A. Foi, "A nonlocal transform-domain filter for volumetric data denoising and reconstruction," IEEE Trans Image Process., vol. 22, no. 1, pp. 119–133, Jan. 2013.

[39] M. Bayati and A. Montanari, "The dynamics of message passing on dense graphs, with applications to compressed sensing," IEEE Trans. Inf. Theory, vol. 57, no. 2, pp. 764–785, Feb. 2011.

[40] A. Manoel, F. Krzakala, E. W. Tramel, and L. Zdeborová, "Sparse estimation with the swept approximated message-passing algorithm," Arxiv preprint arxiv:1406.4311, June 2014.

[41] S. Rangan, A. K. Fletcher, P. Schniter, and U. Kamilov, "Inference for generalized linear models via alternating directions and Bethe free energy minimization," Arxiv preprint arxiv:1501.01797, Jan. 2015.

[42] D. Foster, K. Amano, S. Nascimento, and M. Foster, "Frequency of metamerism in natural scenes," J. Optical Soc. of Amer. A, vol. 23, no. 10, pp. 2359–2372, Oct. 2006.